

Effective bias removal for fringe projection profilometry using the dual-tree complex wavelet transform

William Wai-Lam Ng and Daniel Pak-Kong Lun*

Centre for Signal Processing, Department of Electronic and Information Engineering,
The Hong Kong Polytechnic University, Hong Kong, China

*Corresponding author: enpkun@polyu.edu.hk

Received 4 May 2012; revised 18 July 2012; accepted 20 July 2012;
posted 23 July 2012 (Doc. ID 168016); published 16 August 2012

When reconstructing the three-dimensional (3D) object height profile using the fringe projection profilometry (FPP) technique, the light intensity reflected from the object surface can yield abruptly changing bias in the captured fringe image, which leads to severe reconstruction error. The traditional approach tries to remove the bias by suppressing the zero spectrum of the fringe image. It is based on the assumption that the aliasing between the frequency spectrum of the bias, which is around the zero frequency, and the frequency spectrum of the fringe is negligible. This, however, is not the case in practice. In this paper, we propose a novel (to our knowledge) technique to eliminate the bias in the fringe image using the dual-tree complex wavelet transform (DT-CWT). The new approach successfully identifies the features of bias, fringe, and noise in the DT-CWT domain, which allows the bias to be effectively extracted from a noisy fringe image. Experimental results show that the proposed algorithm is superior to the traditional methods and facilitates accurate reconstruction of objects' 3D models. © 2012 Optical Society of America
OCIS codes: 120.2650, 100.7410.

1. Introduction

Fringe projection profilometry (FPP) is a popular technique for noncontact three-dimensional (3D) object profile measurement [1–6]. In FPP, a fringe pattern is first projected onto the target object. Due to the variation of the object's height profile, the fringe pattern is deformed as seen on the object surface. Such deformation provides sufficient information for reconstructing the 3D shape of the object [1]. In practice, the deformed fringe pattern is captured by a digital camera and can be formulated as follows:

$$I(x, y) = a(x, y) + b(x, y) \cos[2\pi f_o x + \varphi(x, y)] + n(x, y), \quad (1)$$

where I is the captured fringe image, f_o is the fundamental frequency of the sinusoidal fringe

pattern in the x direction, a is the bias, b is the fringe amplitude, φ is the phase shift of the sinusoidal fringe pattern in the x and y directions, and $n \sim N(0, \sigma^2)$ is the additive noise with a normal distribution. If φ is known, the height profile of the object can be readily estimated [1]. However, the estimation of φ is not trivial, particularly when the captured fringe image I has a strong bias and is contaminated by noise. Recently, our team proposed a new (to our knowledge) fringe image enhancement algorithm that effectively recovers the fringe pattern from a noisy image [2]. It makes use of the dual-tree complex wavelet transform (DT-CWT) [7], which converts the fringe pattern in the image to a piecewise smooth function in the transform domain. In this case, the edge preserving smoothing algorithm can be performed to remove the noise in the transform coefficients. The algorithm adopted the phase shift profilometry (PSP) technique [3] such that the bias is removed before the enhancement process. However,

the PSP approach requires two or more fringe images captured in sequence, which is not suitable for fast moving objects. A bias removal algorithm that uses a single fringe image is more desirable.

In fact, the bias $a(x,y)$ in Eq. (1) is introduced by the light intensity reflected from the object surface. It can have abrupt changes in magnitude due to, for instance, the abrupt changes of the color pattern of the object. It should be removed or severe distortion will occur in the reconstructed 3D height profile. As the bias appears to be at zero spectrum (ZS) in the frequency domain, one traditional approach tries to remove the ZS by applying a high pass filter in the Fourier domain [1]. However, such an approach assumes that the aliasing between the ZS and higher order harmonics of the image is negligible, which is not true in general. In [8], the continuous wavelet transform was used to filter out the bias. It exploits the correlation of the image among adjacent rows. Another recent attempt for eliminating the bias used empirical mode decomposition (EMD) [9]. The EMD is designed to adaptively shape the data into intrinsic mode functions (IMFs) through sifting iterations. The resulting IMFs are made to be as symmetric as possible around zero, which implies they are unbiased. However, both approaches fail to eliminate local bias with sharp changes in magnitude, which are often found in real fringe images.

In this paper, a novel (to our knowledge) bias removal algorithm is proposed. The new approach works in the DT-CWT domain such that it can be easily integrated into [2] to allow effective bias removal and denoising at the same time. The proposed approach successfully identifies the features of bias, fringe, and noise in the DT-CWT domain such that the bias can be effectively extracted out from a noisy fringe image. Experimental results show that the proposed method is superior to the existing methods such as FT and EMD, particularly when the fringe image has sharp changes in bias magnitude or the noise level is high. It has a performance comparable with using the traditional PSP approach when the object is static, and it improves significantly when the object is moving.

2. Proposed Method

In [2], an efficient algorithm using the oriented two-dimensional (2D) DT-CWT is proposed for enhancing noisy fringe images. To explain the algorithm, let us first rewrite Eq. (1) as follows:

$$I = g + n = W^+ I_w = W^+(g_w + n_w), \quad (2)$$

where W^+ is the inverse oriented 2D DT-CWT, I and g are the observed fringe image and the clean fringe image with bias, respectively, n is defined as in Eq. (1), and $I_w, g_w,$ and n_w are the wavelet coefficients of $I, g,$ and $n,$ respectively. It is shown in [2] that due to the special features of DT-CWT, the magnitude of g_w exhibits a piecewise smooth response such that an edge preserving smoothing operator can be applied

to I_w to reduce the noise. However, if g contains strong bias, the denoising procedure in [2] is not sufficient to handle the resulting irregularity introduced to g_w . Severe distortion may result in the reconstructed 3D height profile. As mentioned above, we propose in this paper a new algorithm to reduce the bias in the fringe image. The new algorithm operates in the DT-CWT domain to facilitate easy integration into [2]. Let the edge preserving smoothing operator in [2] be denoted as Ψ . Then assume there is another operator ϑ in the DT-CWT domain that can detect the bias in the fringe image. The whole fringe image enhancement algorithm can be described as follows:

$$\begin{aligned} \tilde{I} &= W^+(\Psi(WI^f)) = W^+(\Psi(W(I - W^+\vartheta(WI)))) \\ &= W^+(\Psi(g_w + n_w - \vartheta(g_w + n_w))), \end{aligned} \quad (3)$$

where I^f refers to a bias free fringe image. Equation (3) shows that due to the orthogonality of the DT-CWT, the proposed bias removal algorithm can be implemented within [2] without extra forward or inverse transformations. To explain the proposed bias removal operator ϑ , let us provide further definition:

$$I_w^l = a_w^l + f_w^l + n_w^l, \quad (4)$$

where $I_w^l, a_w^l, f_w^l,$ and n_w^l are the respective level l wavelet coefficients; $l = 1, 2, \dots, L$. Note that they are complex numbers defined in the context of the DT-CWT. Our task is to extract a_w^l from I_w^l by removing f_w^l and n_w^l as much as possible. Similar to the traditional DT-CWT based denoising techniques, we work on the magnitude response of I_w^l defined as follows:

$$\begin{aligned} |I_w^l|^2 &= |a_w^l + f_w^l + n_w^l|^2 = |a_w^l|^2 + |f_w^l|^2 + |n_w^l|^2 \\ &\quad + 2 * \text{real}(a_w^l f_w^{l*} + a_w^l n_w^{l*} + f_w^l n_w^{l*}), \end{aligned} \quad (5)$$

where x^* is the complex conjugate of x . It is known that the fringe f is a narrowband signal with energy that can only be found in some of the subbands. In fact, the number of subbands that contain fringe energy has a close relationship with the rate of change of the object's height profile. It is shown in Appendix A that if $h(x,y)$ is the height profile of the object, d is the distance between the camera and the projector, and s is the distance between the projector and the object, the energy of the fringe can only be found in subbands from l_{\min} to l_{\max} such that

$$l_{\min} = \left\lfloor \log_2 \left(\frac{1}{(f_o/f_s)(1-d/s)(\Delta h)_{\max}} \right) \right\rfloor, \quad (6)$$

$$l_{\max} = \left\lceil \log_2 \left(\frac{1}{2(f_o/f_s)(1-d/s)(\Delta h)_{\min}} \right) \right\rceil, \quad (7)$$

where $\Delta h = \partial h(x, y) / \partial x$ and f_s is the sampling frequency. Equations (6) and (7) show that the number of subbands that contain fringe energy can be easily determined if we have a rough knowledge of the maximum and minimum rate of change (in x -direction) of the object's height profile. We do not need to have an exact knowledge of them, since a slight error in their estimation would only lead to a slight error in the estimation of the maximum and minimum frequency components of the fringe signal. Therefore, as long as the estimated ones and the true ones are in the same frequency subband, the same conclusion will be made regarding the subbands that contain fringe energy. Even in the boundary case that the estimated ones are in the next subbands from the true ones, only a small amount of fringe frequency components will be missed. In general it would not significantly affect the final reconstructed image. Note that in theory, Eqs. (6) and (7) apply only to vertical subbands, as indicated in Appendix A. For simplicity, we also apply the results of Eqs. (6) and (7) to the computation of horizontal and diagonal subbands. Our experimental results show that in general they do not introduce adverse effects to the final results.

For subbands that do not have significant f_w^l , it is known from Eq. (5) that

$$E\{|I_w^l|^2\} = E\{|a_w^l|^2\} + E\{|n_w^l|^2\}, \quad (8)$$

where $E\{\cdot\}$ is the expectation function. Equation (8) shows that the estimation of a_w^l is a typical denoising problem of the DT-CWT. Since the bias $a(x, y)$ is the light intensity reflected from the object surface, its magnitude can be represented by some step functions connected by smooth functions in the spatial domain. Due to the vanishing moments of the dual-tree complex wavelets [7], the response of the smooth functions will vanish while the step functions will incur impulses in the DT-CWT domain. On the other hand, the wavelet coefficients of noise will scatter with small magnitude in the transform domain. Hence, the bias wavelet coefficients a_w^l can be extracted from I_w^l by using a soft-thresholding scheme as follows:

$$|\hat{I}_w^l| \cong \max(|I_w^l| - \lambda, 0) \quad \text{for } l \text{ with negligible } f_w^l. \quad (9)$$

The threshold λ needs to be carefully selected. Since $n \sim N(0, \sigma^2)$, it can be shown that its magnitude response in the DT-CWT domain becomes Rayleigh distributed with $\text{std} = \sqrt{(4 - \pi) * 2\sigma^2 / 2}$ and $\mu = \sqrt{2\sigma^2 \pi / 2}$. The following threshold λ is thus selected to ensure the noise wavelet coefficients are sufficiently suppressed:

$$\lambda = \mu + 3 * \text{std}. \quad (10)$$

A different procedure is used for the other subbands that contain significant f_w^l . Referring to Eq. (5), $|I_w^l|^2$ in these subbands is composed of $|a_w^l|^2$, $|f_w^l|^2$, and $|n_w^l|^2$ and some cross terms that have relatively smaller magnitude. As shown in [2], $|f_w^l|^2$

is the only piecewise smooth function in $|I_w^l|^2$, while the others are either spurious or random. Hence we can make a rough estimation of $|f_w^l|^2$ by applying a median filter to $|I_w^l|$ as follows:

$$(\text{med}\{|I_w^l|\})^2 \cong |f_w^l|^2 + E(|n_w^l|^2) = |f_w^l|^2 + 4\sigma^2. \quad (11)$$

Therefore,

$$|I_w^l|^2 - (\text{med}\{|I_w^l|\})^2 + 4\sigma^2 \cong |\tilde{a}_w^l|^2 + |n_w^l|^2 + 2 \times \text{real}(f_w^l n_w^{l*}), \quad (12)$$

where $|\tilde{a}_w^l|^2 = |a_w^l|^2 + 2 \times \text{real}(a_w^l f_w^{l*} + a_w^l n_w^{l*})$. Again, the estimation of $|\tilde{a}_w^l|$ in these subbands becomes a typical denoising problem of the DT-CWT and can be achieved by applying Eq. (9). Note that, similar to $|a_w^l|^2$, the term $2 \times \text{real}(a_w^l f_w^{l*} + a_w^l n_w^{l*})$ is highly localized, that is, nonzero, only around the rising or falling edges of the bias $a(x, y)$. However, it has a much smaller magnitude than $|a_w^l|^2$. So $|\tilde{a}_w^l|$ can be considered as $|a_w^l|$ with slight distortion, which can be handled in the subsequent denoising process [2].

After the magnitude response of the DT-CWT coefficients is processed, it can be combined with the original phase response to form the complex coefficients as follows:

$$\hat{I}_w^l = \vartheta(WI) = |\hat{I}_w^l| \exp(-j\angle I_w^l). \quad (13)$$

They can then be applied back to Eq. (3) for further 3D model reconstruction.

3. Results and Discussion

Simulations were conducted to compare the performance of the proposal bias removal algorithm with the traditional approaches. In these simulations, the fringe pattern of a testing object (Fig. 1) is generated as shown in Fig. 2. A bias pattern is arbitrarily designed and added to the fringe pattern as shown in Fig. 3. In the figure, the magnitude of the bias is indicated by its brightness. We scale the bias pattern such that the ratio between the maximum change of the bias magnitude and the fringe magnitude

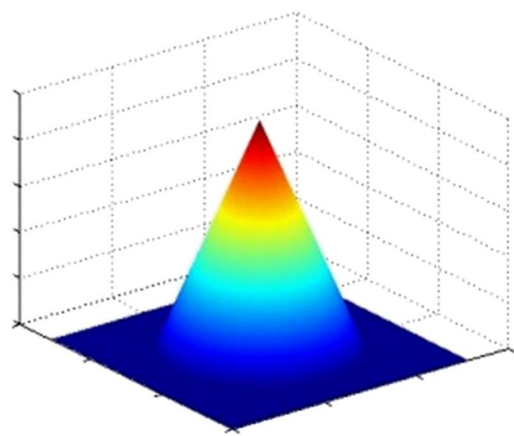


Fig. 1. (Color online) Testing object.

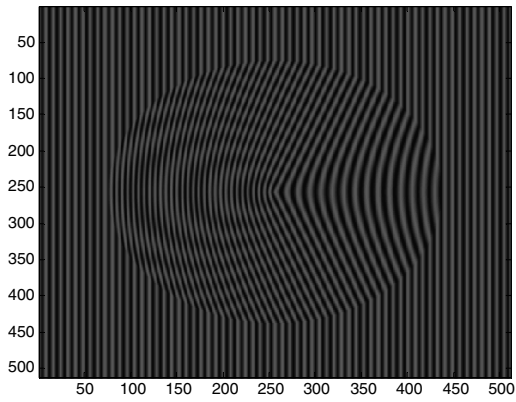


Fig. 2. Computed fringe of the testing object.

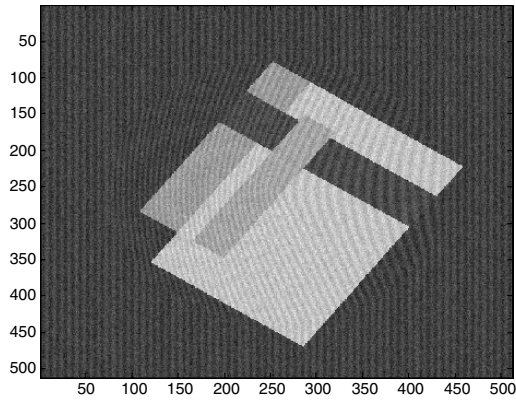


Fig. 3. Biased and noisy fringe ($\beta = 10$, $\sigma^2 = 1$).

(denoted as $\beta = \frac{|\partial a / \partial x|_{\max}}{b}$) is from 5 to 15. White Gaussian noises of different noise variance ($\sigma^2 = 0.5$ to 2.0) are then added to the biased fringe images. Figure 4 shows one slice (row #256) of the biased ($\beta = 10$) and noisy fringe ($\sigma^2 = 1$). Different algorithms (FT [1], EMD [9], and the proposed) are used to remove the bias in the image. Figure 5 shows the bias in the same slice (row #256) as in Fig. 4 estimated using the proposed algorithm. It can be seen that the bias is accurately estimated. The resulting fringe images are then further denoised using the approach in [2]. The enhanced images are processed

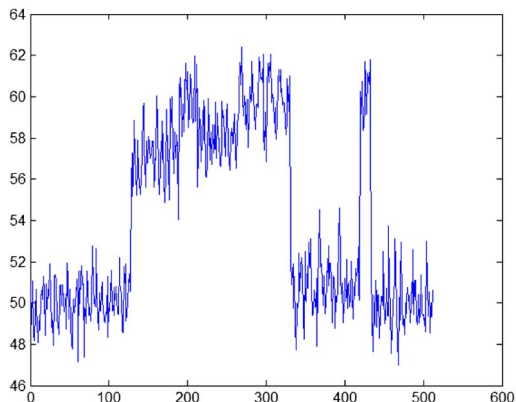


Fig. 4. (Color online) Row #256 of Fig. 3.

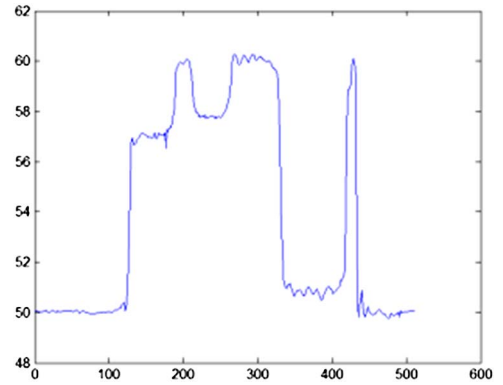


Fig. 5. (Color online) Bias extracted using the proposed algorithm.

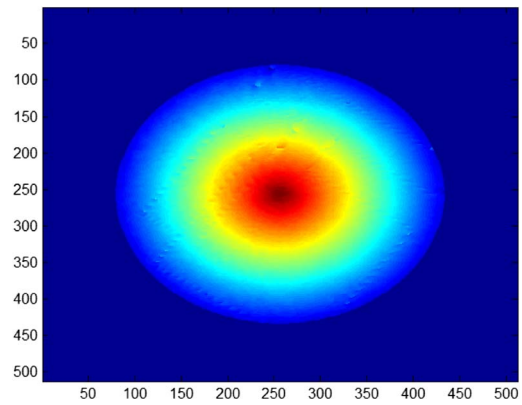


Fig. 6. (Color online) Reconstructed 3D model using the proposed algorithm.

with Goldstein's phase unwrapping technique [10] to estimate the phase. Finally, the 3D model of the target object is reconstructed. Figures 6–8 show the end results. Compared with the traditional approaches, the reconstructed 3D model using the proposed bias removal algorithm contains much less defect. Table 1 shows a comparison between the three approaches at different β and σ^2 . It can be seen that the proposed algorithm consistently outperforms the traditional approaches. The difference is particularly significant at high σ^2 and large β .

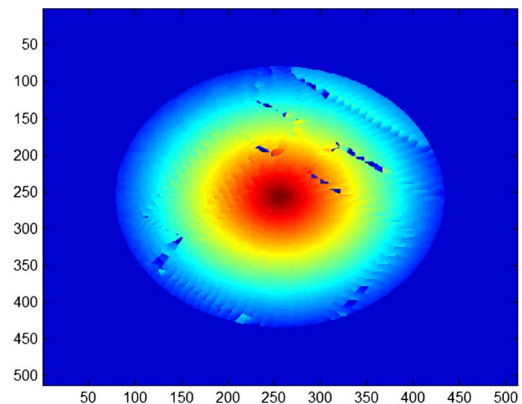


Fig. 7. (Color online) Reconstructed 3D model using the FT approach.

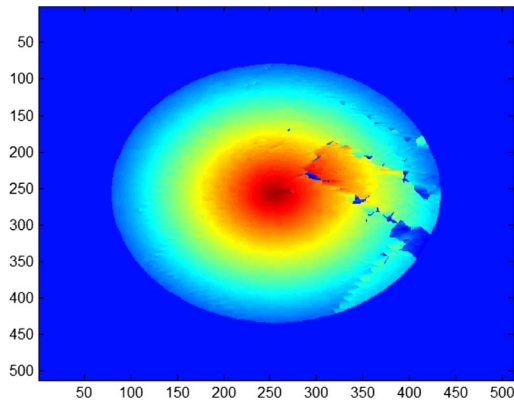


Fig. 8. (Color online) Reconstructed 3D model using the EMD approach.

We further test the proposed algorithm with a real object and compare this with different approaches. We first project a fringe pattern onto a paper airplane as shown in Fig. 9. Then the deformed fringe image is captured using a digital single lens reflex (SLR) camera. As can be seen in Fig. 10, the color patterns on the object induce bias on the captured fringe images, which should be removed as much as possible before reconstruction. Figures 11–13 show the reconstructed 3D model after using different bias

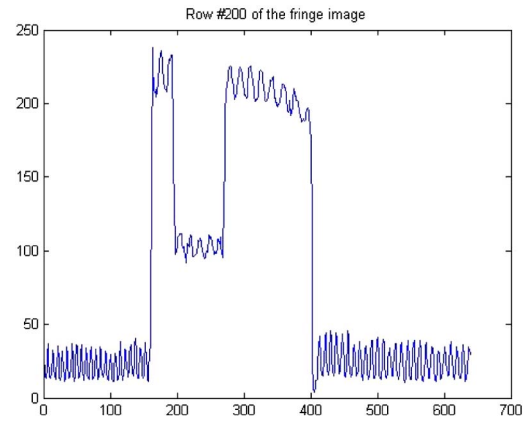


Fig. 10. (Color online) Row #200 of the fringe image.

removal approaches: FT, EMD, and the proposed approach, respectively. Apparently, the proposed approach gives a much better result. Finally, we also show in Figs. 14 and 15 the results of using the PSP technique for static and moving objects, respectively. It can be seen in Fig. 14 that the proposed algorithm can yield an output comparable to using PSP if the object is static. However, when the object is slightly moved between the instants that the

Table 1. Comparison of the Reconstructed 3D Models in Terms of Mean Square Error (mse) after Using Different Bias Removal Algorithms at Different Noise Levels and Bias Magnitudes

		Noise Level σ^2			
		0.5	1	1.5	2
Proposed	β 5	9.80	9.86	9.93	10.26
	10	9.84	9.88	10.02	10.44
	15	9.88	9.96	10.10	10.82
FT [1]	β 5	9.85	9.90	9.95	10.19
	10	16.02	17.73	15.23	17.46
	15	45.09	32.88	34.42	39.05
EMD [9]	β 5	9.83	11.93	34.55	68.07
	10	15.36	29.40	52.83	71.55
	15	32.95	46.52	66.26	89.11

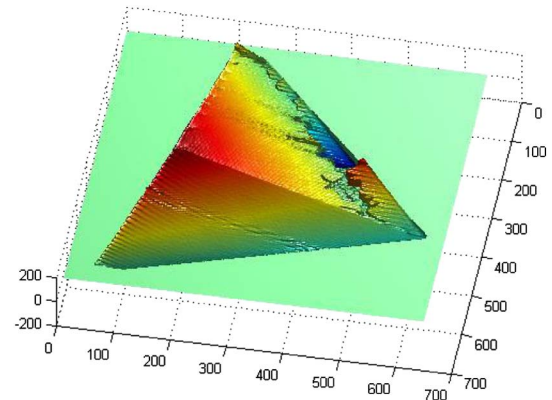


Fig. 11. (Color online) Reconstructed 3D model using the FT approach.

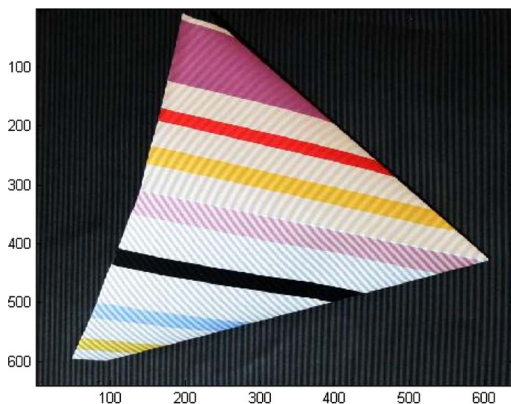


Fig. 9. (Color online) Testing the real object with the fringe projected.

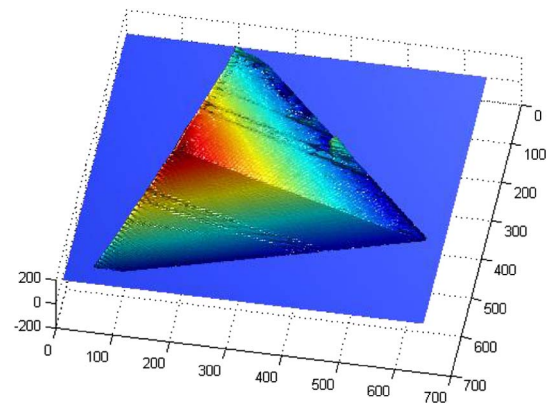


Fig. 12. (Color online) Reconstructed 3D model using the EMD approach.

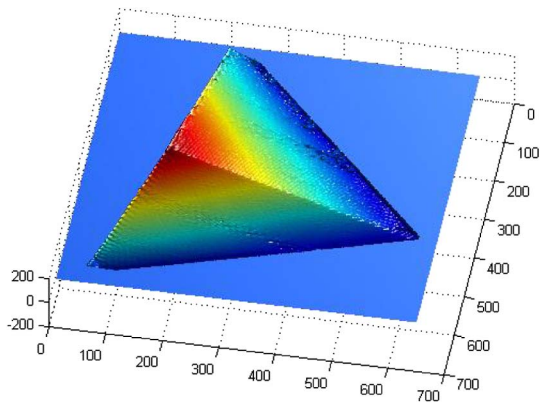


Fig. 13. (Color online) Reconstructed 3D model using the proposed algorithm.

two images are captured, the second fringe image does not align well with the first one, which leads to severe reconstruction error, as can be seen in the experimental result in Fig. 15. Another real object example is shown in Fig. 16. Figures 17–19 show

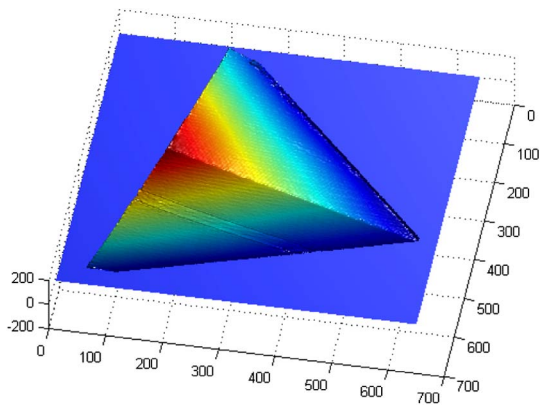


Fig. 14. (Color online) Reconstructed 3D model using the PSP approach. The object is static when capturing the two fringe images.

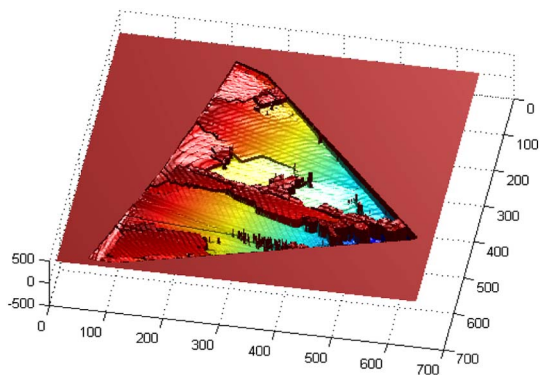


Fig. 15. (Color online) Reconstructed 3D model using the PSP approach. The object is slightly moved when capturing the two fringe images.

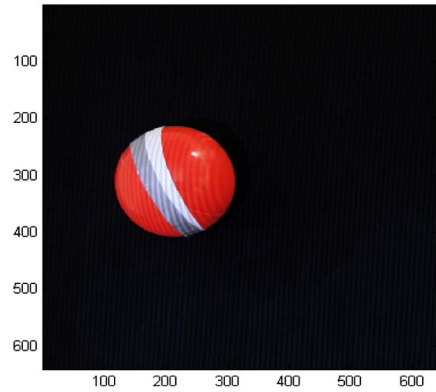


Fig. 16. (Color online) Ball object with fringe projected.

the reconstructed 3D models of the object in Fig. 16 after using different bias removal approaches: FT, EMD, and the proposed approach, respectively. Significant improvement is also noted as compared with the traditional approaches. The result shows the generality of the proposed algorithm.

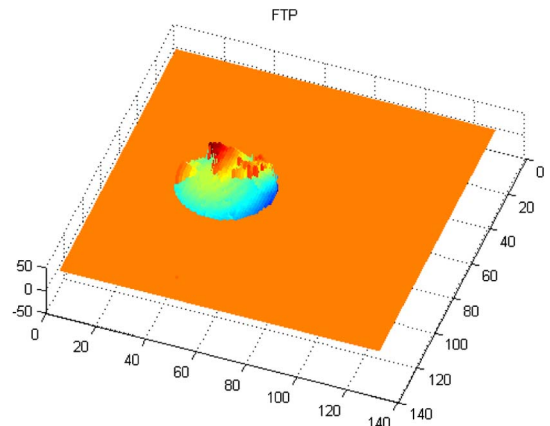


Fig. 17. (Color online) Reconstructed 3D model using the FT approach.

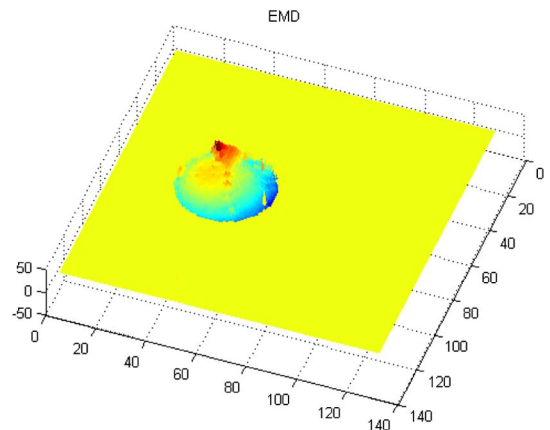


Fig. 18. (Color online) Reconstructed 3D model using the EMD approach.

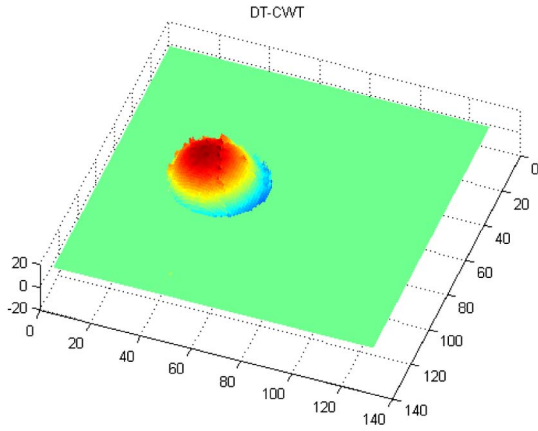


Fig. 19. (Color online) Reconstructed 3D model using the proposed algorithm.

4. Conclusion

In this paper, an effective bias removal algorithm is proposed for FPP. The new algorithm works in the DT-CWT domain, which allows easy integration into the previous approach to enable bias removal and denoising to be carried out at the same time. In the DT-CWT domain, the bias can be described by some impulses, which are very different from the wavelet coefficients of fringe and noise. To allow effective extraction of those impulses, we first identify the subbands that do not contain fringe energy so that simple soft thresholding can be applied. For those subbands that contain fringe energy, a median filter is used, followed by a soft-thresholding procedure, to remove the fringe energy and noise, respectively. Although some distortion may be introduced to the resulting bias coefficients, they can be handled by the subsequent denoising process. A series of simulations and experiments were conducted to verify the proposed algorithm. Significant improvement is noted compared with the traditional FT and EMD approaches, particularly when the fringe image has sharp changes in bias magnitude or the noise level is high. It has a performance comparable with using the traditional PSP approach when the object is static, but it improves significantly when the object is moving.

Appendix A

In fringe projection profilometry, the phase $\varphi(x, y)$ is related to the height $h(x, y)$ of an object by $\varphi(x, y) = -2\pi f_0 h(x, y) d/s$, where s is the distance between the camera and the projector; d is the distance between the projector and the object; and f_0 is the fundamental frequency. For each slice of the fringe image g_y , it is known [1] that its energy concentrates at the first harmonic with spectral boundaries as follows:

$$\text{BW}(g_y) \approx \left\{ f_0 + \frac{1}{2\pi} \left(\frac{\partial \varphi(x, y)}{\partial x} \right)_{\min}, f_0 + \frac{1}{2\pi} \left(\frac{\partial \varphi(x, y)}{\partial x} \right)_{\max} \right\}, \quad (\text{A1})$$

where $\text{BW}(g_y)$ denotes the bandwidth of g_y , and $\left(\frac{\partial \varphi(x, y)}{\partial x} \right)_{\min}$ and $\left(\frac{\partial \varphi(x, y)}{\partial x} \right)_{\max}$ are the minimum and maximum rate of change, respectively, of the phase $\varphi(x, y)$ in the x direction. Note that $\left(\frac{\partial \varphi(x, y)}{\partial x} \right)_{\min}$ is a negative number. Now assume that the fringe image is transformed using the DT-CWT. Let us first consider the wavelet coefficients in the vertical subbands, which capture mainly the change of the signal in the x direction. Since the DT-CWT is constructed by half-band filters, the bandwidth of each slice of transform coefficients in vertical subbands w_l^V can be roughly defined as follows:

$$\text{BW}(w_l^V) = \left\{ \frac{f_s}{2^{l+1}}, \frac{f_s}{2^l} \right\}, \quad (\text{A2})$$

where f_s is the sampling frequency and $l = 1, 2, \dots, L$. As shown in Eq. (A1), the energy of each slice of the fringe image will not go beyond its upper and lower spectral boundaries. Hence, after applying the DT-CWT, it will concentrate in only some of the vertical subbands from level l_{\min} to l_{\max} , which can be determined by

$$\begin{aligned} \frac{f_s}{2^{l_{\min}}} &\geq f_0 + \frac{1}{2\pi} \left(\frac{\partial \varphi}{\partial x} \right)_{\max}, \\ \frac{1}{2^{l_{\min}}} &\geq \frac{1}{f_s} \left(f_0 + \frac{1}{2\pi} \left(\frac{\partial}{\partial x} \left(\frac{-2\pi f_0 d \cdot h(x, y)}{s} \right) \right)_{\max} \right), \\ l_{\min} &= \left\lfloor \log_2 \left(\frac{1}{(f_0/f_s)(1-d/s) \left(\left(\frac{\partial h(x, y)}{\partial x} \right)_{\max} \right)} \right) \right\rfloor. \end{aligned} \quad (\text{A3})$$

Similarly, l_{\max} can be determined as follows:

$$\begin{aligned} \frac{f_s}{2^{l_{\max}+1}} &\leq f_0 + \frac{1}{2\pi} \left(\frac{\partial \varphi}{\partial x} \right)_{\min}, \\ l_{\max} &= \left\lceil \log_2 \left(\frac{1}{2(f_0/f_s)(1-d/s) \left(\left(\frac{\partial h(x, y)}{\partial x} \right)_{\min} \right)} \right) \right\rceil. \end{aligned} \quad (\text{A4})$$

Note that in theory, Eqs. (A3) and (A4) apply only to the vertical subbands. For simplicity, we assume the horizontal and diagonal subbands also have the same l_{\min} and l_{\max} . In general this does not significantly affect the final result. This is because the horizontal and diagonal subbands usually have much less fringe energy than the vertical subbands, such that $l_{\max}^V \geq l_{\max}^D, l_{\max}^H$ and $l_{\min}^V \leq l_{\min}^D, l_{\min}^H$, where V , D , and H refer to vertical, diagonal, and horizontal subbands. Hence, when using the same l_{\min} and l_{\max} for the horizontal and diagonal subbands, it is possible that we may also apply the proposed bias removal and denoising algorithm to diagonal or

horizontal subbands that contain no fringe energy. This, however, does not significantly affect the overall performance, although the computational complexity can be slightly increased.

This work is supported by the Hong Kong Polytechnic University under research grant G-U862.

References

1. M. Takeda and K. Mutoh, "Fourier transform profilometry for the automatic measurement of 3-D object shapes," *Appl. Opt.* **22**, 3977–3982 (1983).
2. T. C. Hsung, D. P. K. Lun, and W. W. L. Ng, "efficient fringe image enhancement based on dual-tree complex wavelet transform," *Appl. Opt.* **50**, 3973–3986 (2011).
3. X. Su and W. Chen, "Fourier transform profilometry: a review," *Opt. Lasers Eng.* **35**, 263–284 (2001).
4. J. Zhong and J. Weng, "Spatial carrier-fringe pattern analysis by means of wavelet transform," *Appl. Opt.* **43**, 4993–4998 (2004).
5. S. Li, X. Su, and W. J. Chen, "Spatial carrier fringe pattern demodulation by use of a two-dimensional real wavelet," *Appl. Opt.* **48**, 6893–6906 (2009).
6. K. Qian, "Windowed Fourier transform for fringe pattern analysis," *Appl. Opt.* **43**, 2695–2702 (2004).
7. I. W. Selesnick, R. G. Baraniuk, and N. G. Kingsbury, "The dual-tree complex wavelet transform," *IEEE Signal Process. Mag.* **22**(6), 123–151 (2005).
8. M. A. Gdeisat, D. R. Burton, and M. J. Lalor, "Eliminating the zero spectrum in Fourier transform profilometry using a two-dimensional continuous wavelet transform," *Opt. Commun.* **266**, 482–489 (2006).
9. S. Li, X. Su, W. Chen, and L. Xiang, "Eliminating the zero spectrum in Fourier transform profilometry using empirical mode decomposition," *J. Opt. Soc. Am. A* **26**, 1195–1201 (2009).
10. D. C. Ghiglia and M. D. Pritt, *Two-Dimensional Phase Unwrapping: Theory, Algorithms, and Software* (Wiley, 1998).